

Prediction of the Unsteady Flow Field in a Turbine including Air Seal Cavities with Time and Frequency Domain Methods

Maximilian Hartmann *1, Marcel Oettinger¹, Daniel Schlüβ¹, Georg Geiser², and Florian Herbst²

¹MTU Aero Engines AG, Dachauer Straße 665, 80995 Munich, Germany ²Institute of Propulsion Technology, German Aerospace Center (DLR), Linder Höhe, 51147 Cologne, Germany

Abstract

In recent years, the effects of side geometries, such as air seal cavities, have gained increasing attention in the design process of modern turbomachinery. This study investigates the hypothesis that radial mixing effects by these geometries significantly influence performance metrics and radial temperature distributions. In order to identify the fidelity level necessary to predict these effects accurately results of steady and unsteady Computational Fluid Dynamics (CFD) simulations are compared to experimental data of a 1.5-stage turbine with inner and outer air seal cavities. In particular state-of-the-art steady simulations are compared with high-fidelity unsteady time-domain simulations and an unsteady frequency-domain Harmonic Balance (HB) method. The latter being recently extended for such configurations with a novel sliding mesh approach. The results demonstrate that the inclusion of the cavity geometries in the computational setup increases the prediction quality for all three numerical approaches. However, only with both unsteady approaches an excellent agreement with experimental performance metrics and radial temperature distributions is achieved. The HB method requires one order of magnitude less computationally resources than the time-domain approach. The results allow for the conclusion that the accurate prediction of radial mixing processes requires the inclusion of side geometries as well as unsteady blade row interactions. Being as accurate but significantly more efficient than the time-domain method HB enables the improvement of industrial design processes with regard to such effects.

Keywords: Unsteady turbine flow, Cavities, Harmonic Balance

1 Introduction

In the field of turbomachinery design and analysis, computation fluid dynamics (CFD) simulations have emerged as a crucial tool for predicting and improving the performance in a wide range of applications. The increasing complexity of methods for the unsteady flow simulation has become a demanding field today. Moreover, with the availability of more computational resources, there is a growing demand for incorporating more realistic geometries, such as inner and outer air seal cavities. These cavities can play a significant role in the overall performance and efficiency of turbomachinery systems in terms of aerodynamics, which can expressed by a shift in the operating point. Furthermore, unsteady methods are essential in the field of aeroelastic analyses, such as flutter or forced response calculations.

To combine these challenges of computational expensive unsteady simulations and the urge to incorporate side geometries like cavities, we show the application of different methods in the time and frequency domain using a novel implementation of a sliding mesh interface to connect the cavities to the main flow channel [1, 2]. In the frequency domain, we use the Harmonic Balance (HB) method that assumes a temporally and spatially periodic unsteady flow field. The studies of Kluge et al. [3] have shown that the investigated rotating cavity induces fluctuations which are non-harmonic w.r.t. the machine's engine order. These fluctuations can only be captured by the HB solver if their corresponding frequencies are exactly defined at the start of the simulation. Unfortunately,

there are only rough empirical estimates for these frequencies, and in most cases, they remain unknown prior to detailed simulations. In contrast to the isolated cavity, it is questionable if these induced non-harmonic fluctuations, which can be described as turbulent large-scale structures, can build up under the forced pressure fluctuations of the rotor by incorporating the whole turbine with cavities.

Furthermore, the cavity flow often exhibits significantly lower velocities and Mach numbers when compared to the main flow. For a density-based solver like TRACE, a resolution of these low Mach numbers can be challenging and potentially leads to significantly longer convergence times. Although recent efforts, such as those by Sivel et al. [4], have focused on low-Mach number preconditioning, particularly for the HB solver, no preconditioning was applied in this work.

This paper is organized as follows: Section 2 details the numerical methods employed in this study. Section 3 describes the test case, providing all necessary information. In Section 4, we compare the CFD results across different numerical setups and validate them against experimental data where possible. Finally, Section 5 presents our conclusions, discusses the significance of our results for current turbomachinery designs, and highlights potential directions for future research.

2 Numerical methods

The TRACE turbomachinery research and design code, jointly developed by MTU Aero Engines and the German Aerospace Center (DLR) [5], is used for the CFD simulations in this study. TRACE employs a finite volume approach to solve

^{*}Corresponding author: maximilian.hartmann@mtu.de

the three-dimensional compressible Favre-averaged Navier-Stokes equations with a density based update, on both structured and unstructured multi-block meshes. Convective fluxes are discretized by Roe's second-order accurate upwind scheme with MUSCL extrapolation. To enhance the solution smoothness near shocks, a modified van Albada limiter is applied. Additionally, diffusive fluxes are discretized using a central difference scheme that incorporates mixed derivatives. Turbulence is modeled by Wilcox' two-equation eddy viscosity model [6]. This model solves the transport of the turbulent kinetic energy k and turbulent dissipation rate ω . The Kato-Launder modification prevents the unphysical overproduction of k in flow stagnation regions [7].

An additional model is applied to account for turbulent transition effects. Previous studies using the multi-mode transition model by Kozulovic [8] in the HB solver revealed a poor convergence behavior. Therefore, a two-equation γ - Re_{Θ} model by Müller-Schindewolffs [9] is employed that allows for robust simulations in the frequency domain. It is applied to all walls, except in the cavities.

In the main flow domain, all boundary layers on viscous walls are discretized by a mesh that captures the laminar sublayer without using any wall functions. Inside the cavities, viscous walls are modeled with wall functions. At the in- and outlet boundaries, non-reflecting boundary conditions formulated in the frequency domain are applied in all simulations, as these methods can be used for the time-domain solver as well as for HB [10, 11]. This ensures a consistent comparison between both methods.

2.1 URANS in time domain

The URANS simulations in the time domain are conducted using an implicit Euler backward time discretization scheme. Because of its implicit formulation, a CFL number of 200 can be applied. To capture also the harmonics of the highest engine orders, generated by the row with the highest blade count, we have chosen to resolve one blade passing period with 90 time steps. This results in 540 time steps for one passing of the 60 deg segment. Each of these time steps contains up to 40 inner pseudo-time iterations.

Quasi-steady convergence is assessed by monitoring the local flow values at several locations in the main flow and within the cavities. These signals are analyzed using a Discrete Fourier Transform (DFT) over one segment passing period, similar to the work of Clark and Grover [12].

Starting from a steady-state initial solution, the unsteady time-domain simulations converged after approximately 40 segment passing periods. This long convergence time is caused by a relatively small drift in the time-averaged values that was observed at the outlet plane.

2.2 Harmonic Balance

The HB solver within TRACE has proven to be highly effective in simulating unsteady flow fields, frequently offering a more efficient alternative to conventional time-domain methods in various applications [13]. It solves the quasisteady RANS equations for a given set of solution harmonics using an alternating time and frequency domain algorithm.

Table 1: Rig geometric and operating parameters.

| Rotational speed in 1/min Mass-flow rate in kg s ⁻¹ Total pressure ratio | | 7000 9.20 1.42 | |
|---|--------|----------------------|--------|
| Blade count Aspect ratio $Re = \frac{cC_{ax}}{v}$ | Vane 1 | Rotor | Vane 2 |
| | 18 | 30 | 36 |
| | 2.15 | 2.15 | 2.15 |
| | 79 900 | 65 000 | 42 900 |

This approach allows the general transport equations, as well as boundary conditions, to be consistently applied in both solvers. The consistency between these two modes is unique to the HB method and enables a direct and reliable comparison between the conventional time-domain solver and the HB solver. The HB calculations have been initialized by a converged steady RANS solution. To incorporate the fluctuations of the turbulent model quantities in a numerically stable manner, a Lanczos filter method is applied in all HB calculations [14]. A CFL number of five was employed for the pseudo-time step, as using higher values resulted in a destabilization of the solver. All sliding mesh interfaces use the latest implementation by Geiser et al. [1] for both simulation types in time and frequency domain. First successful applications of this interface have been presented by Hartmann et al. [2].

3 Test case

The test case is based on a 1.5-stage low-pressure turbine investigated previously by Oettinger et al. [15, 16]. Compared to these previous investigations, the present configuration features a new rotor cavity design that is more representative of a straight-through labyrinth seal in aero engines (cf. Figure 1). Details on this new configuration are given in the work of Lohse et al. [17] who used it to derive an acoustic scaling method. We use the "large-gap" configuration with an axial gap between the vanes and the rotor of $X/C_{\rm ax}=80\%$. The measurements for the new casing cavity have been conducted at identical operating points when compared to previous works. A summary of key geometric and operating parameters is given in Table 1. The geometry of the cavities is shown in Figure 1 and is not the focus of this work. Due to confidentiality reasons, detailed geometry data cannot be published.

3.1 Instrumentation

The instrumentation concept is described in detail by Oettinger et al. [16]. Here, only a summary focusing on additional instrumentation and key features for the numerical validation is given. In measurement plane (MP) 2.10, the two-dimensional turbine inlet flow field is measured across a circumferential segment of 30 deg which equals half of the strut pitch and contains the strut wake. Additional radial traverses at 0 deg and 60 deg allow for an extrapolation to a full strut pitch. In addition to pneumatic five-hole probe traverses, hotwire anemometry is used to measure turbulence intensities and

Table 2: Overview of CFD setups.

| Setup | Description | Cavities |
|------------|----------------------------|----------|
| A1 | RANS in time domain | no |
| B1 | URANS in time domain | no |
| C 1 | HB in frequency domain, v1 | no |
| D1 | HB in frequency domain, v2 | no |
| A2 | RANS in time domain | yes |
| B2 | URANS in time domain | yes |
| C2 | HB in frequency domain, v1 | yes |
| D2 | HB in frequency domain, v2 | yes |

length scales. Five rake probes in MP 3.02 allow to determine the outlet total pressure and total temperature. Local three-hole probe measurements additionally provide the outlet flow angle and pressure. Vanes 1 and 2 are instrumented with pressure taps at mid-span. Vane 2 has additional pressure taps at $r_{\rm rel} = 90\%$.

Both the inlet and outlet chambers of the outer cavity feature unsteady pressure measurements (Kulite XCQ-062). One pressure transducer is located in the inlet chamber. The outlet chamber uses a staggered positioning of four taps across 58 deg.

3.2 Numerical setup

The main flow domain mesh is identical to the one used by Oettinger et al. [16]. At all walls the mesh resolution is able to resolve the laminar sub-layer of the boundary layer in the main flow domain. The cavity mesh is attached using a sliding-mesh interface. This mesh is not wall-resolved; here, a wall-function formulation of the turbulence model is used instead.

The circumferentially averaged inlet boundary condition is obtained from the measurements in MP 2.10. At the outlet, the static pressure is iterated until the total pressure ratio of the experiment is matched by the steady-state simulations. Here, the total pressure ratio was calculated using the circumferentially averaged total pressure at the Euler radius at MP 2.10 and MP 3.02. This procedere was done for both steady simulations, with and without cavities and the same outlet pressure is applied in all unsteady simulations. For all unsteady, time and frequency domain, simulations the value obtained in steady-state simulations is prescribed.

To investigate the influence of the cavity flow and the impact on the main flow, two different setups are considered, which are further refined by the different methods used. In the first set, the cavity is neglected while it is included in the second set. A complete overview of all investigated numerical setups and their abbreviations is given in Table 2. Each geometry was simulated using four different numerical methods and setups. The time domain simulations were conducted using both a steady RANS approach and a dual-time stepping method as described in Section 2.1. The rotor-stator interfaces in the main flow are consistently modeled using a mixing plane approach [18], except for setup B, which features multiple passages in each domain.

In this case, all domains have the same circumferential pitch, so there is no need for a phase shift for the sliding

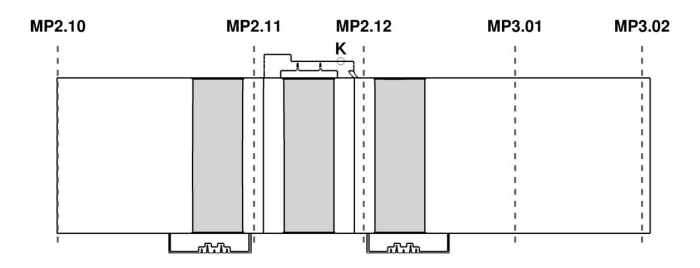


Figure 1: Turbine rig geometry with measurement planes and axial position of Kulite sensors K.

mesh approach. The interfaces between the main flow and the cavities are entirely in radial direction. Previous studies have shown that in such secondary flow directions, the mixing plane approach is insufficient to capture the flow interactions between the two domains. Therefore, in each setup, the sliding mesh interface approach is used to interpolate the local flow field in both directions, without any circumferential averaging. The position of the interfaces for the rotor domain with OAS can be seen in Figure 7.

Figure 1 shows the geometry of the turbine with two inner air seal (IAS) cavities at the hub of each stator and an outer air seal (OAS) cavity at the shroud of the rotor. This OAS is identical to the geometry of the rotating labyrinth test facility in Hanover, which has been investigated in previous studies [3]. The measurement planes are named by MP. In this study, we focus on the analysis of MP 2.12 right before the second stator and MP 3.02 at the outlet.

In the HB method, harmonic sets are defined by a base frequency and its higher harmonics, along with the inter-blade phase angle (IBPA), which describes the phase shift between the pitch of the disturbance source domain and the actual domain. The specific harmonics used in the simulation are listed in Table 3. As noted in previous experimental studies [15] the first three harmonics of the neighboring domain's blade or vane passing frequencies are the most significant sources of unsteady pressure disturbances. In this work, all downstream disturbances are resolved using four harmonics. Since the vane count ratio between stator 1 and 2 is exactly two, the upstream effects of stator 2 can be captured using the same base frequency as stator 1. As a result, the rotor domain can capture four harmonics of stator 1 and three harmonics of stator 2. All domains, related to cavities, have only one neighboring domain, so the harmonic sets are identical to those of the connected main flow domain.

The only difference between HB setups C and D is the IBPA, which is set to $120 \deg$ (Setup D) instead of $60 \deg$ (Setup C) due to the pitch ratio between rotor and stator 2. By using two passages of stator 2, the pitch becomes equal to that of stator 1, allowing the disturbances from stator 1 to be captured by the 0th harmonic flow solution. This is a current limitation of the sliding interface because clocking modes with an IBPA of $\pm 180 \deg$ result in Fourier coefficients with only a real part such that the imaginary part of the spatial Fourier transform cannot be determined.

Table 3: Harmonic sets of HB Setups C/D. Setup D has a different IBPA of 120 deg.

| Domain | Base frequency | Harmonics | IBPA [deg] |
|--------------|------------------|-----------|------------|
| Stator 1 | BPF ₁ | 01234 | 120 |
| Rotor 1 | VPF_1 | 012346 | -144 |
| Stator 2 | BPF_1 | 0 1 2 3 4 | 60 (120) |
| IAS 1 | BPF_1 | 01234 | 120 |
| OAS (rot) | VPF_1 | 012346 | -144 |
| OAS (nonrot) | BPF_1 | 01234 | 60 (120) |
| IAS 2 | BPF_1 | 0 1 2 3 4 | 60 (120) |
| | | | |

4 Results and discussion

4.1 Time-averaged results

In this section, we present the time-averaged results at the selected operating point. The comparison between the turbine configurations with and without cavities clearly shows that it is very important to take the cavities into account in the analysis. As can be seen in Figure 2a all transient simulations show a higher pressure ratio, but the deviations are not significant compared to a relative deviation of 0.2% from the experimental pressure ratio. In this representation, all values are normalized by the results from the measurement data. Setup D was designed to achieve better consistency with the TD-URANS reference, which is confirmed when comparing the total pressure ratio results of both B2 and D2.

Next to the pressure ratio, we evaluate the isentropic efficiency in Figure 2b. The isentropic efficiency of a turbine is the ratio of the actual total enthalpy change to the maximum possible enthalpy change, assuming an isentropic process:

$$\eta_{\rm is} = \frac{\Delta h_t}{\Delta h_{t \, \rm is}} \tag{1}$$

For an ideal gas this simplifies to:

$$\eta_{\rm is} = \frac{T_{t2} - T_{t1}}{T_{t2\rm is} - T_{t1}} = \frac{\frac{T_{t2}}{T_{t1}} - 1}{\left(\frac{p_{t2}}{p_{t1}}\right)(\gamma - 1)/\gamma - 1}$$
(2)

In the present simulations without cavities, the isentropic efficiency decreases by around 1.5% due to transient effects. Additionally, the presence of cavities results in a further efficiency reduction of approximately 3%. Nevertheless, while the efficiency still deviates from the reference, the divergence is notably smaller than that observed in the steady-state results. By considering the meausrement tolerance of 1.66%, only the unsteady methods with cavity are able to predict the isentropic efficiency from the experiment.

To further investigate the effects of the OAS cavity, the time-averaged pressure on the surfaces of the stator 2 vanes was analyzed and is illustrated in Figure 3 at two different channel heights. The static pressure is non-dimensionalized using the pressure coefficient

$$c_p = \frac{p - p_{\text{out}}}{p_{t,\text{in}} - p_{\text{out}}} \tag{3}$$

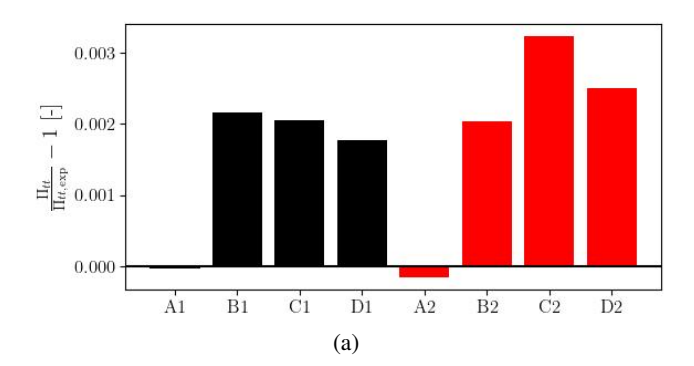
which incorporates the total pressure at the inlet of the machine $p_{t,\rm in}$ and the static pressure at the outlet of the row $p_{\rm out}$. Both reference pressures are evaluated at the Euler radius (54% of channel height) that separates the channel into two equally sized areas.

The impact of the OAS is stronger at a channel height of 90%. The cavity ejects fluid into the main flow, directly impacting stator 2. The most significant differences occur at the leading edge and the first half of the suction side, due to a change in the flow angle at the leading edge. The fluid emitted from the OAS has a lower momentum than the main flow and is not significantly deflected by the rotor. Although the maximum pressure values remain almost unchanged when considering the cavities, the pressure distribution shifts, resulting in higher pressure on the suction side, particularly in the first halft of the vane. There is an agreement between the experimental data and the CFD results for the configuration with cavities. However, there are some noticeable deviations at the suction side, that cannot be attributed to measurement tolerances, which are not higher than the shown symbols.

But even at mid-span, the pressure profile on the suction side changes significantly due to the cavity influence. Between the steady and unsteady methods, only a relatively small deviation is observed. In this context, HB setup C that neglects clocking effects is more similar to the steady setup A. However, the resolution of the clocking effect of stator 1 on stator 2 in HB setup D results in a very good agreement with the unsteady setup B. The clocking effect is also highlighted in Figure 5 that will be discussed later. The results are consistent with the findings of Oettinger et al. [16], as the present configuration describes the "large-gap" case in their investigations. Due to the comparatively large gap, the influence of unsteady wake-boundary-layer interactions on the loading is relatively small. In comparison to the experimental data, minor deviations are observed at the suction side. However, the results demonstrate a strong agreement at the leading edge and the entire pressure side.

Figure 4 shows the radial temperature distribution predicted by the different simulation methods. The radial profile becomes more uniform, where both low and high temperature extrema are being reduced when using unsteady approaches. When compared to the simulations without cavities, the total temperature is around 5% higher. These temperatures are averaged, weighted by the mass, in the circumferential direction across the entire computational domain. For setups A and C, the averaging is performed over a single passage of stator 2. In setup B, the averaging is done over six passages, while in setup D, it is performed over two passages. The higher temperatures at the shroud surface are caused by hot fluid ejected from the OAS. This is also observed in the measurement data and there is a sufficient agreement between simulation and experiment at the shroud. At mid-span the unsteady simulations predict temperature distributions that are much closer to experimental data when compared to steady simulation results. However, the distinct temperature peak at the hub has not been observed in the experiment and this deviation also cannot be explained by measurement tolerances. This is still under investigation.

The investigated numerical methods exhibit similar behav-



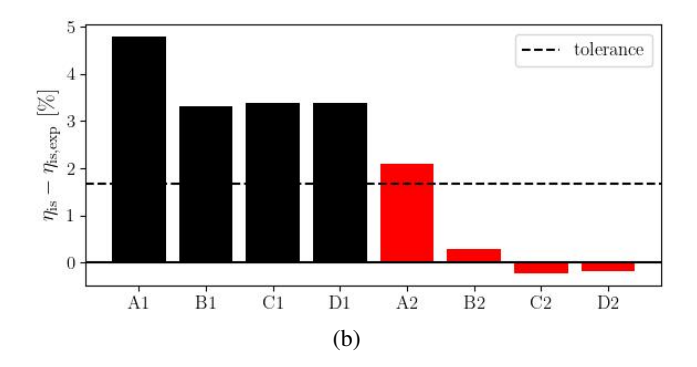


Figure 2: Global performance values between MP 2.10 and MP 3.02. (a) Total pressure ratio, (b) Isentropic efficiency.

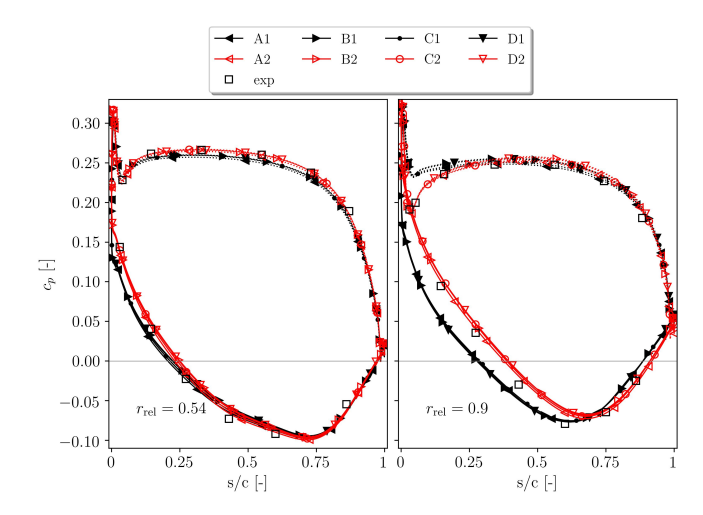


Figure 3: Time-averaged surface pressure coefficient for stator 2 at mid-span (Left) and close to the tip (Right).

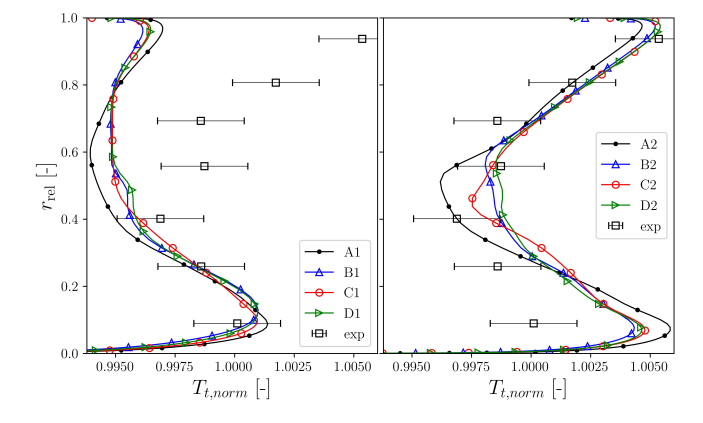


Figure 4: Time- and circumferentially-averaged normalized total temperature over the channel height at MP 3.02. Without cavities (Left), with cavities (Right).

ior for both machine configurations, with the greatest differences observed between the steady setup A and the unsteady variants. Although the deviations in temperature are well below 1%, setup B shows an increase in the minimum temperature at mid-channel and a decrease in the temperature peaks close to the hub. Notice that both HB setups are also able to predict this behavior. Furthermore, incorporating the disturbances from stator 1 on stator 2 (setup D) leads to a clear improvement in matching time-domain URANS reference data (setup B). The lower temperature at the shroud in setup A2 is probably caused by the steady mixing plane interface between OAS, rotor and stator 2. Only the transient interfaces used in the unsteady simulation can accurately predict the mixing processes in the hot fluid at the shroud.

Although the differences between HB setups C and D are not significant in the fluid temperature distributions, the resolved clocking effect is clearly noticeable in the time-averaged flow field. Figure 5 highlights vortical flow structures and radial flow from the OAS into the main channel by depicting the radial component of the fluid velocity vector at MP 2.12. This velocity is normalized by a consistent value across all setups, ensuring that disturbances remain within approximately $\pm 1.$ For comparison purposes, the data is periodically duplicated in circumferential direction to allow a direct comparison between all setups.

A distinct pattern of three is observed in the lower half of the channel in both reference results B1 and B2 ①. This pattern corresponds to a wave number of 18 over the entire circumference, caused by the number of vanes in the stator 1 (see Table 1). It is clearly generated by the three stator 1 vanes over the 60 deg domain in time-domain URANS simulation and can only be captured by HB setup D, which accounts for the downstream disturbances of stator 1 that affect stator 2. In the configuration with cavities, a larger region of flow in negative radial direction is observed, driven by the bleed flow from the OAS into the main flow. This region ② exhibits a wave number of 36, caused by the interaction with the potential pressure field of the downstream stator.

When comparing setups A and C, the pattern with a wave number of 36 is again observed, but with varying intensity. If this pattern were solely caused by the potential field of stator 2, there should not be any noticeable difference. However, the flow is already affected by the second harmonic of the stator 1 disturbance in the rotor, which is then transported into the stator 2 domain. Moreover, in setup D2, the wave number of 18 is more present in the upper region 2, whereas setup B2 shows a more distinctive pattern of 36 (3).

4.2 Instantaneous results

To gain deeper insight into the differences between the numerical methods, an analysis of the instantaneous flow fields is conducted.

Figure 6 illustrates the row interactions by normalized entropy contours at mid-span. Apparently, the wakes induced by the turbomachinery blades are only transported downstream when using unsteady simulation methods.

The outflow region after stator 2 where all flow disturbances interact with each other is of particular interest. The merging entropy trails are only captured by the unsteady methods, which explains why the temperature is less mixed in the radial direction for the steady simulation results in setup A, cf. Figure 4. Between the two HB setups, C and D, the influence of stator 1 on stator 2 can be observed (highlighted by red rectangles). However, even HB setup C represents a significant improvement over the RANS simulation approach.

It is important to note that the novel sliding mesh interface, particularly within the HB method, plays a crucial role in the success of these simulations. In this study, we further validate the accurate transport between the main flow and cavity, ensuring continuity between both domains. To illustrate this, instantaneous total fluid temperature distributions using an absolute frame of reference are shown in Figure 7. For normalization, the same representative value T_{ref} , corresponding to the mean temperature in the experimental data, was used for all results. The angular position is constant, located exactly between two vanes of stator 2, in order to minimize the upstream impact of the potential field. This specific position is indicated in the upper left view, which also denotes the current relative position of the rotor in relation to the stators. It is evident how the fluid expands as it passes through the rotor passage, extracting work and thereby reducing the total temperature. Within the cavity, expansion is not possible, so the hot fluid bypasses the rotor and enters the main flow, eventually reaching stator 2. Nevertheless, the hot streak is only noticeable near the shroud wall. With regard to the validation of the sliding mesh interface, no discontinuities are observed in this representation. The transition between rotating and stationary components is handled seamlessly. When comparing the results of the different numerical setups, a small difference between B2 and the HB results can be observed.

4.3 Frequency spectrum in outer cavity

During the measurement campaign, time-discrete static pressure signals were recorded using Kulite sensors in the OAS, with data being collected at one position near the inlet and at four different circumferential positions in the outlet chamber. The axial position of these sensors is shown in Figure 1. The pressure was measured over a defined, with each time sample corresponding to a specific rotor angle. In total, there are 1700 phase angles covering the full annulus, and each data set is averaged over time. To compare this data with the numerical results, the rotating domain is transformed into the

corresponding absolute frame of reference. The signal is then processed using a discrete Fourier transform (DFT) to obtain the spectrum of pressure fluctuations. The original signal in the time domain and its corresponding spectrum are shown in Figure 8 and Figure 9 along with results from the URANS setup B and Harmonic Balance setups C/D. In terms of frequency domain results, the reconstructed time-domain signal is shown for 1/6th of a revolution. For the URANS simulation and the experiment, a full revolution of the rotor is taken into account for the DFT. Signals from simulations are all converged periodically and show only content at harmonics of the blade passing frequency (BPF). In contrary, the experimental data shows strong fluctuations in amplitude intensity, although the BPF is again captured correctly. Looking at Figure 9, the fluctuations around the time-averaged static pressure value at this specific location are approximately 0.5% in the simulation. The experimental results indicate fluctuations within the range of 0.4% and 1% of the time-averaged static pressure value at this specific location. In Figure 8, all amplitudes are normalized by the same value, which is the highest pressure amplitude at engine order (EO) 30 from the experimental data. The simulated pressure fluctuations are in average lower than the experimental data. Looking at the first BPF harmonic, only simulation C2 shows a significantly lower amplitude. The time-domain simulation B2 predicts a decreased amplitude which is approximately 10% lower than, in the experiment. Surprisingly the HB setup D2 has an even better agreement to the experiment than the time-domain simulation B2. Further, the amplitude at second harmonic is only about 20% the amplitude of the first harmonic. In the case of simulation results, there is no noticeable content in frequencies above EO 90, while experimental data shows some higher pressure amplitudes at 3% to 5%. This approves that the use of only four higher harmonics in the HB simulations can accurately reproduce the results of the time-domain URANS method.

In the case of simulation results, there is no noticeable content in frequencies above EO 90, which agrees fairly well with the experimental data showing low amplitudes from 3% to 5%. This confirms that, at least for the discussed test case, the use of only four higher harmonics in the HB simulations can accurately reproduce the results of the time-domain URANS method.

4.4 Computational costs

One major advantage in using the frequency domain methods is the reduction in computational costs. In this study, we compare a highly resolved time-domain simulation with two different HB simulations, both considering the same number of harmonic solutions, but differing in size of the computational domain of stator 2, where either one or two passages are considered. The computational costs, in terms of CPU time, and the number of volume elements for each numerical setup are summarized in Table 4. Notice that these values strongly depend on the convergence rate of the solver. Overall, the computational effort for the time-domain simulations is $\mathcal{O}(100)$ higher than for a steady RANS simulation, while the HB method is only $\mathcal{O}(10)$ more expensive.

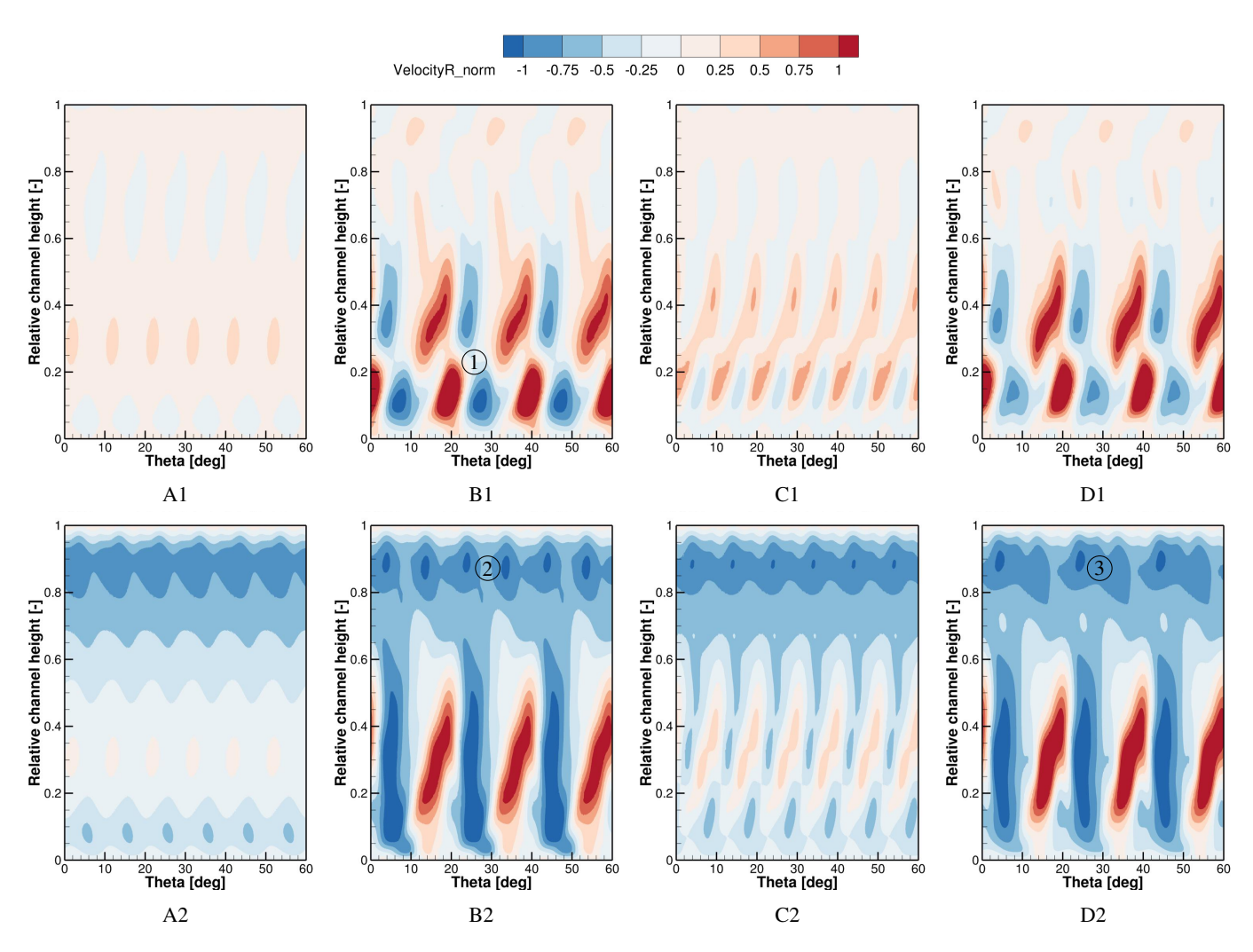


Figure 5: Time-averaged radial flow velocity component at MP 2.12. Results are normalized using the same reference value for every setup.

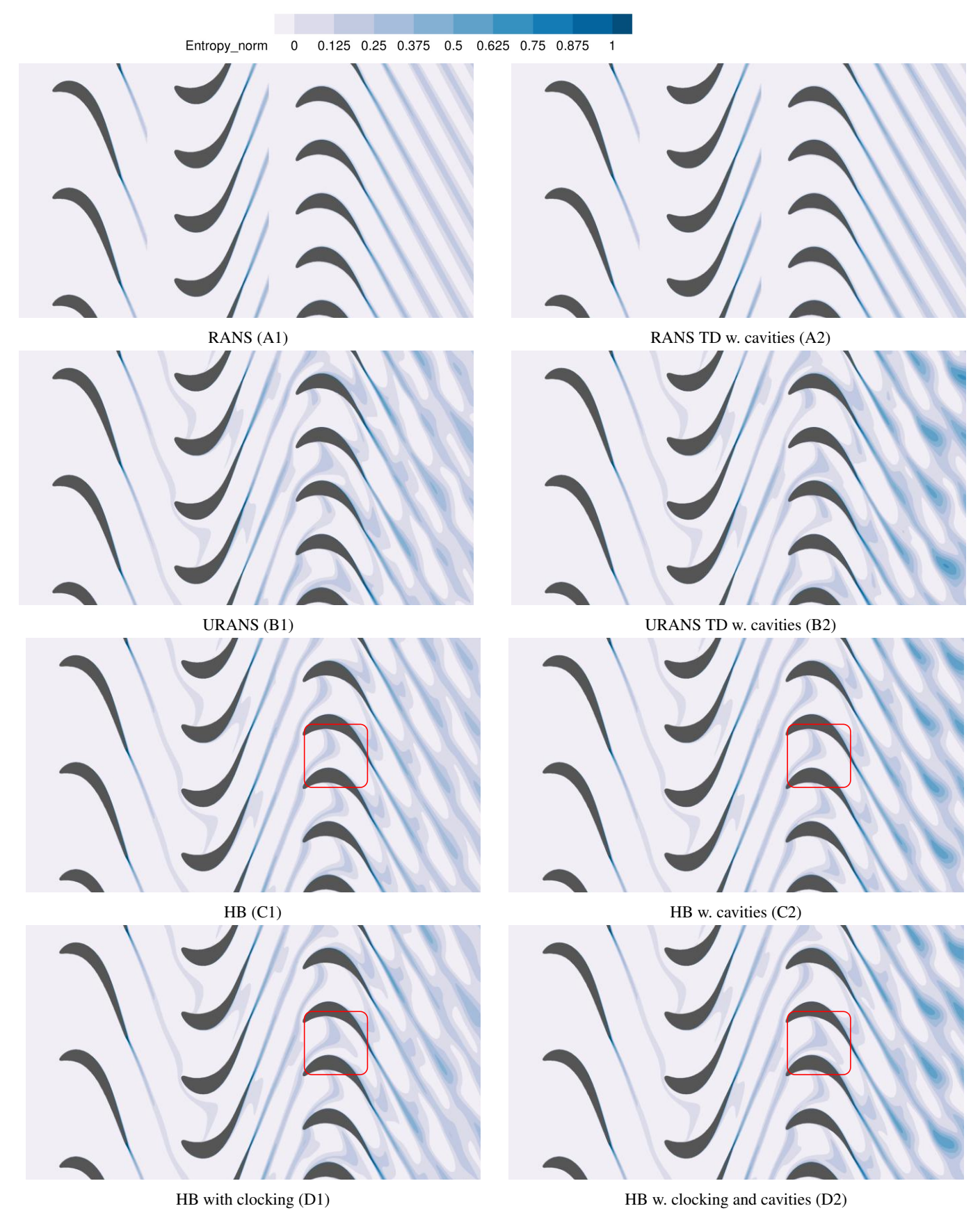


Figure 6: Normalized fluid entropy contours at mid-span S1 surfaces. Results are instantaneous, except for RANS.

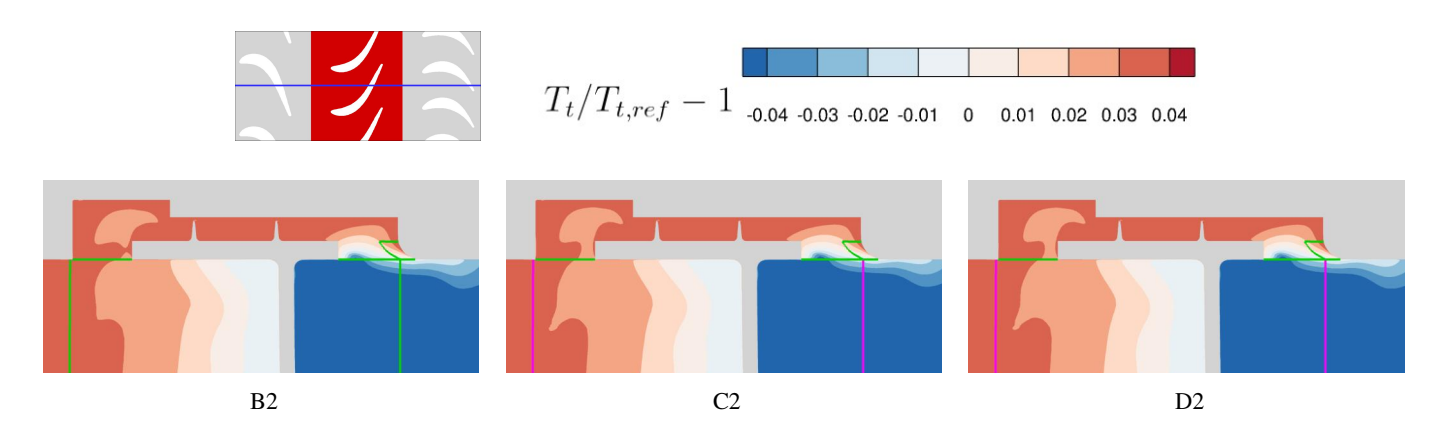


Figure 7: Instantaneous normalized total fluid temperature distributions in a $\theta = \text{const.}$ plane using the absolute frame of reference. Interfaces are highlighted: Sliding mesh interface (green) and HB mixing plane approach (purple).

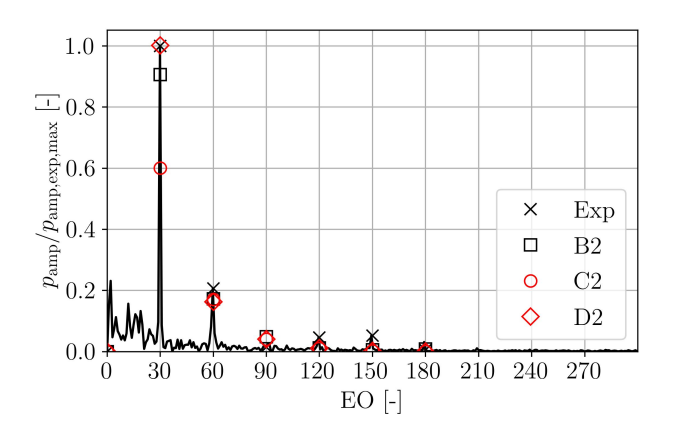


Figure 8: DFT of the static pressure in the outer air seal cavity. Line is only shown for experimental data, because simulations provide only multiples of EO.

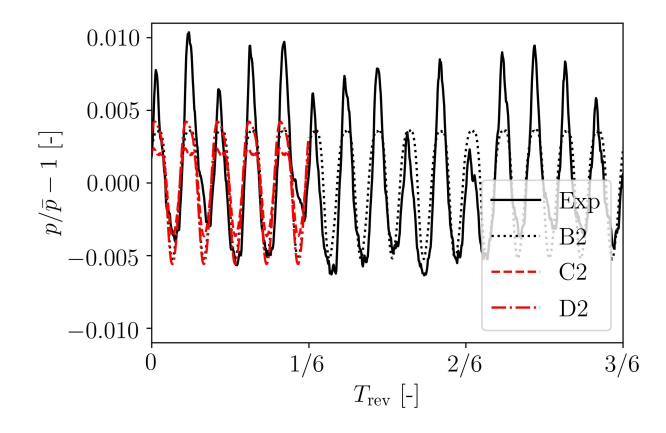


Figure 9: Time signal of the static pressure in the outer air seal cavity.

Table 4: Computational costs of time and frequency domain methods for cavity setups.

| Setup | Normalized CPU time | Grid elements |
|-------|---------------------|---------------------|
| A2 | 1 | 1.2×10^{7} |
| B2 | 171 | 5.7×10^{7} |
| C2 | 15 | 1.2×10^{7} |
| D2 | 21 | 1.7×10^{7} |

5 Conclusions

Simulation results of a turbine rig at the design operating point with and without cavities were investigated. Different computational methods in the time and frequency domain were used to analyze the unsteady flow field in the outlet region of the OAS. We compared the Harmonic Balance (HB) method with conventional unsteady Reynolds-averaged Navier–Stokes (URANS) methods to evaluate their accuracy and efficiency. By examining the computational demands and ability to capture key flow characteristics, we highlighted the strengths and limitations of each approach.

The main findings of this study are:

- First of all, the ability to conduct unsteady simulations with the HB method for main flow and cavity geometries is shown.
- The study shows that unsteady methods are necessary to capture specific aspects, such as accurate radial temperature profiles.
- There is good agreement between time domain and frequency domain methods, demonstrating the accuracy and consistency of both approaches.
- While the instantaneous influence of stator 1 on stator 2 is visible in an instantaneous view, it has a relatively minor impact on the overall machine performance.
- The Harmonic Balance (HB) method offers a significant reduction in computational effort, by a factor of around 10 when compared to conventional URANS simulations in the time domain.

• Unlike former investigations of the isolated OAS, no non-harmonic frequencies were observed in the time domain reference simulations in this study. Therefore, the HB method can be effectively applied without the need to account for additional non-harmonic frequencies.

Thus, it can be concluded:

- The HB method, with its newly implemented sliding mesh interface, successfully replicates the results of conventional URANS methods, which were used as the benchmark besides experimental data within this work.
- The HB method can be employed without concerns of introducing new or potential non-synchronous vibrations, making it a robust and reliable approach for this type of analysis.

Future research directions in aeroelastic analysis could involve the utilization of Harmonic Balance simulations for configurations like the presented one. While the differences between steady and unsteady simulations may not be significantly high in the presented test case, it is important to recognize the crucial role of unsteady methods in future applications. In particular, aeroelastic investigations such as forced response or flutter analysis inherently involve unsteady effects, making advanced unsteady methods essential.

As the demand for accurate and reliable simulations in these areas grows, the use of advanced unsteady methods will be essential to capture the complex interactions and dynamic effects that influence the overall performance and stability of turbomachinery.

Acknowledgments

We would like to thank every involved colleague at MTU and DLR for their support and great interest in this work.

Nomenclature

c chord length [m]

 c_p Pressure coefficient [-]

f Frequency [Hz]

m Circumferential wave number [-]

N Blade count [-]

p Static pressure [Pa]

s/c Relative chord length [-]

Temperature, [K]

t Time [sec]

Re Reynolds number [-]

Greek symbols

 η Efficiency

γ Isentropic coefficient / Intermittency in turbulence

transition

v kinematic viscosity

Subscripts

amp Amplitude

is Isentropic

max Maximum

norm Normalized value

R,S Rotor, Stator

ref Reference

t Stagnation quantity (total)

Acronyms

BPF Blade Passing Frequency

CFD Computational Fluid Dynamics

HB Harmonic Balance

IAS Inner Air-Seal cavity

IBPA Inter-Blade Phase Angle

LE Leading Edge

OAS Outer Air-Seal cavity

TD Time Domain

TE Trailing Edge

VPF Vane Passing Frequency

References

- [1] G. Geiser, F. Schwarzenthal, G. Ashcroft, M. Hartmann, and D. Schlüß. "On the Development of an Efficient Sliding Mesh Interface for the Harmonic Balance Method, Part I: Implementation and Verification". In: vol. Volume 12C: Turbomachinery Design Methods and CFD Modeling for Turbomachinery; Ducts, Noise, and Component Interactions. Turbo Expo: Power for Land, Sea, and Air. June 2024, V12CT32A021. DOI: 10.1115/GT2024-125015.
- [2] M. Hartmann, D. Schlüß, G. Geiser, F. Schwarzenthal, G. Ashcroft, and F. Herbst. "On the Development of an Efficient Sliding Mesh Interface for the Harmonic Balance Method, Part II: Effects of Casing Treatments on the Aerodynamic Damping of a Compressor Blade". In: vol. Volume 12C: Turbomachinery Design Methods and CFD Modeling for Turbomachinery; Ducts, Noise, and Component Interactions. Turbo Expo: Power for Land, Sea, and Air. June 2024, V12CT32A033. DOI: 10.1115/GT2024-127237.

- [3] T. Kluge, I. Lettmann, M. Oettinger, L. Wein, and J. Seume. "Unsteady flow phenomena in turbine shroud cavities". In: *Journal of the Global Power and Propulsion Society* 5 (Oct. 2021), pp. 177–190. DOI: 10.33737/jgpps/141211.
- [4] P. Sivel, C. Frey, H.-P. Kersken, and E. Kügeler. "A Low Mach Preconditioned Harmonic Balance Solver for Cavity Flutter Computations". In: vol. Volume 10A: Structures and Dynamics Aerodynamics Excitation and Damping; Bearing and Seal Dynamics; Emerging Methods in Engineering Design, Analysis, and Additive Manufacturing. Turbo Expo: Power for Land, Sea, and Air. June 2024, V10AT21A012. DOI: 10.1115/GT2024-127337.
- [5] M. Franke, E. Kügeler, and D. Nürnberger. "Das DLR-Verfahren TRACE: Moderne Simulationstechniken für Turbomaschinenströmungen". In: DGLR-Jahrbuch. Ed. by DGLR. 2005.
- [6] D. C. Wilcox. "Reassessment of the Scale-Determining Equation for Advanced Turbulence Models". In: *AIAA Journal* 26.11 (Nov. 1988), pp. 1299–1310. DOI: 10. 2514/3.10041.
- [7] M. Kato and B. E. Launder. "The modeling of turbulent flow around stationary and vibrating square cylinders". In: *9th Symposium on Turbulent Shear Flows*. 1993, pp. 10.4.1–10.4.6.
- [8] D. Kozulovic. Application of a Multimode Transition Model to Turbomachinery Flows. Ed. by K. D. Papailiou, F. Martelli, and M. Manna. Mar. 2007.
- [9] C. Müller-Schindewolffs. "Entwicklung eines Modells zur Vorhersage stationärer Transitionsmechanismen in Niederdruckturbinen unter dem Einsatz von skalenauflösenden Simulationen." In: Institut für Turbomaschinen und Fluid-Dynamik, 2021 (Berichte aus dem Institut für Turbomaschinen und Fluid-Dynamik; 28). Chap. 28, p. 203. DOI: 10.15488/11982.
- [10] H.-P. Kersken, G. Ashcroft, C. Frey, N. Wolfrum, and D. Korte. "Nonreflecting Boundary Conditions for Aeroelastic Analysis in Time and Frequency Domain 3D RANS Solvers". In: *Proceedings of ASME Turbo Expo* 2014. GT2014-25499. 2014.
- [11] D. Schlüß and C. Frey. "Time domain implementation of a spectral non-reflecting boundary condition for unsteady turbomachinery flows". In: 24th ISABE Conference. Proceedings of the 24th ISABE Conference. May 2019.
- J. P. Clark and E. A. Grover. "Assessing Convergence in Predictions of Periodic-Unsteady Flowfields".
 In: Journal of Turbomachinery 129.4 (Aug. 2006), pp. 740–749. ISSN: 0889-504X. DOI: 10.1115/1.2720504.
- [13] C. Frey, G. Ashcroft, H.-P. Kersken, and C. Voigt. "A Harmonic Balance Technique for Multistage Turbomachinery Applications". In: *Proceedings of ASME Turbo Expo 2014*. GT2014-25230. June 2014. DOI: 10.1115/GT2014-25230.

- [14] J. P. Heners, D. M. Vogt, C. Frey, and G. Ashcroft. "Investigation of the Impact of Unsteady Turbulence Effects on the Aeroelastic Analysis of a Low-Pressure Turbine Rotor Blade". In: *Journal of Turbomachinery* 141.10 (Sept. 2019), p. 100801. ISSN: 0889-504X. DOI: 10.1115/1.4043950.
- [15] M. Oettinger, M. Henke, F. Herbst, and J. Seume. "Axial-Gap Size Effect on the Unsteady Flow Field at Midspan in a 1.5-Stage Low-Pressure Turbine". In: *Proceedings, International Gas Turbine Congress*. Tokyo, Japan, 2019.
- [16] M. Oettinger, D. Mimic, M. Henke, O. Schmunk, and J. Seume. "Loss assessment of the axial-gap size effect in a low-pressure turbine". In: *Journal of the Global Power and Propulsion Society 5 (2021)* 5 (2021), pp. 1–14.
- [17] S. Lohse, J. Schuler, F. Fischer, J. R. Seume, and S. Moreau. "On the Aeroacoustic Scaling of Axial Flow Turbines". In: *International Journal of Gas Turbine, Propulsion and Power Systems* 15.3 (2024), pp. 9–17.
- [18] D. Schlüß, C. Frey, and G. Ashcroft. "Consistent non-refleflecting boundary conditions for both steady and unsteady flow simulations in turbomachinery applicatations". In: *Proceedings of the 7th Europ.* Ed. by M. Papadrakakis, V. Papadopoulos, G. Stefanou, and V. Plevris. June 2016.